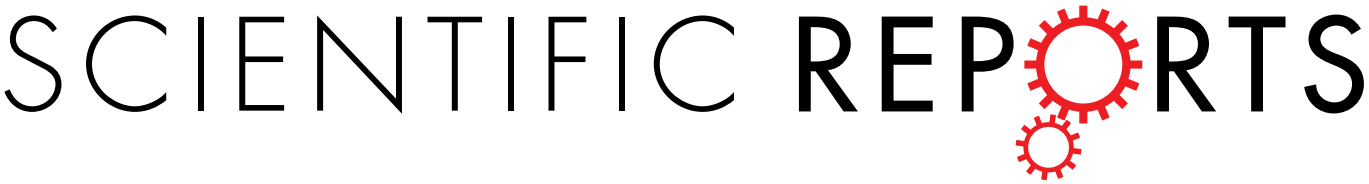

OPEN

Received: 25 May 2016
Accepted: 31 October 2016
Published: 25 November 2016

A universal synthetic route to carbon nanotube/transition metal oxide nano-composites for lithium ion batteries and electrochemical capacitors

Han Zhou[1,*], Lusi Zhang[1,*], Dongyang Zhang[1], Shuangqiang Chen[2], Paul R. Coxon[3], Xiong He[3], Mike Coto[3], Hyun-Kyung Kim[3], Kai Xi[3] & Shujiang Ding[1]

We report a simple synthetic approach to coaxially grow transition metal oxide (TMO) nanostructures on carbon nanotubes (CNT) with ready control of phase and morphology. A thin (~4 nm) sulfonated-polystyrene (SPS) pre-coating is essential for the deposition of transition metal based materials. This layer has abundant sulfonic groups ($-SO_3^-$) that can effectively attract Ni^{2+}, Co^{2+}, Zn^{2+} ions through electrostatic interaction and induce them via hydrolysis, dehydration and recrystallization to form coaxial (NiO, Co_3O_4, $NiCoO_2$ and $ZnCo_2O_4$) shells and a nanosheet-like morphology around CNT. These structures possess a large active surface and enhanced structural robustness when used as electrode materials for lithium-ion batteries (LIBs) and electrochemical capacitors (ECs). As electrodes for LIBs, the $ZnCo_2O_4$@CNT material shows extremely stable cycling performance with a discharge capacity of 1068 mAh g^{-1} after 100 cycles at a current density of 400 mAg^{-1}. For EC applications, the $NiCoO_2$@CNT exhibits a high capacitance of 1360 Fg^{-1} at current densities of 10 Ag^{-1} after 3000 cycles and an overall capacitance loss of only 1.4%. These results demonstrate the potential of such hybrid materials meeting the crucial requirements of cycling stability and high rate capability for energy conversion and storage devices.

The ability to simply design and engineer new materials with tailor-made functionality is an important goal in materials science, and new classes of designer nanoscale materials will likely play a decisive role in the development of future technologies. Carbon nanotubes (CNTs) have received great interest following their discovery by Iijima in 1991[1], owing to their excellent mechanical, thermal, and electrical properties[2–5]. In order to harness the exceptional properties of CNTs, one strategy is to exploit their applications and composite structures with other functional materials, such as polymers, metals and metal oxides/sulfides/nitrides/phosphides[2,3,6–11]. Within these hybrid materials, CNTs typically serve as the support while the functional components fill the cavities and/or are coated on the outer surface[2–4,6,9,10,12–16].

Transition metal oxides (TMOs) as promising functional materials have been widely studied for catalysis applications, gas sensors, energy conversion and storage devices due to their abundance, environmental friendliness and specific physical/chemical properties[4,11,16–19]. However, TMOs typically suffer from poor inherent electrical and ionic conductivities when applied in electrochemical devices such as lithium ion batteries (LIBs) and electro-chemical capacitors (ECs). To address the inherent limitations of TMOs, exciting progress has recently been made in hybridizing TMOs with a conductive matrix[5,20–24]. In particular, hierarchical assembly of TMO nanosheets

[1]Department of Applied Chemistry, School of Science, MOE Key Laboratory for Nonequilibrium Synthesis and Modulation of Condensed Matter, State Key Laboratory for Mechanical Behaviour of Materials, Xi'an Jiaotong University, Xi'an China. [2]Centre for Clean Energy Technology, School of Mathematical and Physical Sciences, University of Technology Sydney, 15 Broadway, Sydney, New South Wales, 2007, Australia. [3]Department of Materials Science and Metallurgy, University of Cambridge, Cambridge CB3 0FS, United Kingdom. *These authors contributed equally to this work. Correspondence and requests for materials should be addressed to K.X. (email: kx210@cam.ac.uk) or S.D. (email: dingsj@mail.xjtu.edu.cn)

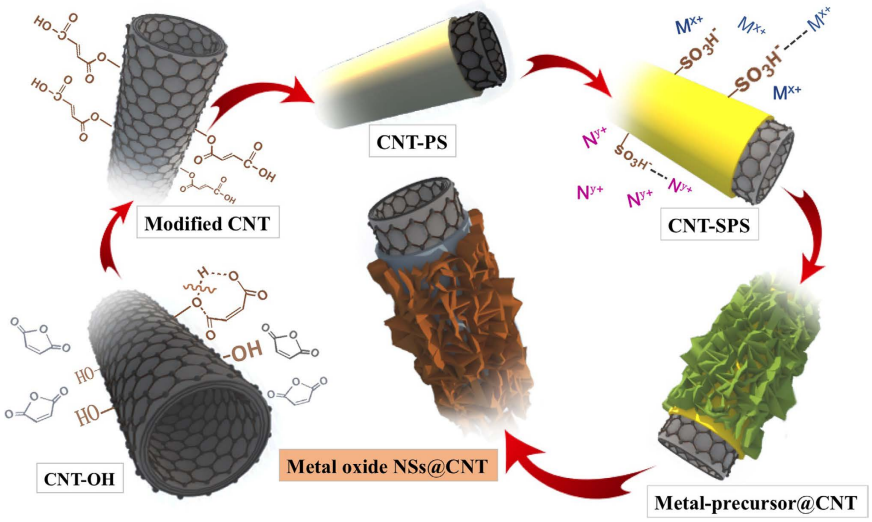

Figure 1. Schematic illustration of the synthetic procedure for TMO@CNT hybrid materials through pre-coating CNT with sulfonated polystyrene.

(NSs) on a framework of CNTs (denoted as TMO@CNT composites) has drawn considerable attention[12,16,25,26]. In industry, the design of a hollow structure inside the nanotube facilitates the conduction of heat, while the lamellar structure outside maximizes the surface area and increases the cooling efficiency[27,28]. Similarly the design of nanosheet sandwich structures with an interior network of carbon nanotubes can enhance the electron transport from within while the outside layer can facilitate ion transport which could bring benefits to applications in various electro-chemical technologies[13,16,25,29–32].

Despite the great potential of these TMO@CNT composites, a general methodology for their controllable synthesis is not yet well established, and it still remains a great challenge to construct high-quality TMO@CNT composite materials in a facile manner. Two characteristics of CNT are considered as major obstacles: they exhibit a strong tendency to agglomerate in order to minimize the total surface free energy and a lack of abundant functional surface groups results in poor compatibility with TMO components[33–36]. Therefore, appropriate surface functionalization is a critical step in the production of delicate hybrid nanostructures. Conventional surface modifications can introduce hydrophilic groups such as –COOH and –OH albeit at the cost of breaking the pristine graphitic CNT structure. Alternative modification approaches for easy growth and/or deposition of inorganic components are highly demanded and the focus of considerable research attention. For example, Du *et al.* attempted to use layer-by-layer assembly to assist the growth of metal oxide layers on CNT, which requires tedious procedures to functionalize the surface of CNT[37] while Yang and coworkers adopted gel polymer inducers to assist the preparation of nanostructured inorganic/polymer composites[38–40]. Previously, we have also applied gel polymers to induce the growth of metal oxide nanosheets to fabricate hollow-structured materials[41,42]. Despite the great progress to date, a universal method to functionalize the surface of CNT and to simultaneously control the coaxial growth of TMO components with morphology control is still absent.

In this work, we have taken inspiration from nature to create hybrid TMO-CNT structures in a simple way with transition metal oxide nanosheets along a carbon nanotube backbone. These structures draw inspiration from lichen and mosses observed growing on bare rocks and bricks. We noticed the growth of lichen position, and found an intermediate layer between the stones and mosses plays an important role for various types of lichen growth (Figure S1). The key of our strategy relies on the pre-coating of a gel polymer layer of sulfonated-polystyrene on the CNT which induces the facile and uniform growth of various TMO nanosheets. Finally, this general synthetic route realized controllable synthesis towards hierarchical hybrid structures composed of CNT backbones and various species of TMO nanosheets, including NiO, Co_3O_4, $NiCoO_2$ and $ZnCo_2O_4$. Owing to the intimate contact between CNT and TMOs and their synergistic effect, the charge transfer process in the hybrid nanostructures is significantly enhanced. As a result, these TMO@CNT composite materials demonstrate excellent electrochemical properties when used as electrode materials in lithium ion batteries and electrochemical capacitors. According to previous reports[20–22], acid treatment was widely used to generate functional groups on the surfaces of CNT, usually via heating CNT in sulfuric/nitric acid at reflux, leading to a large amount of carboxylate ions (–COO–) on the CNT surfaces with negative charge. However, this strategy results in poor morphology control on the as-grown metal oxide nanostructures with unsatisfied coverage of CNT. Herein, we have developed a general strategy for coaxial growth of various transition metal oxide (TMO) nanostructures on CNT by pre-coating a sulfonated polystyrene (SPS). The scheme is illustrated in Fig. 1. CNT with −OH groups (denoted as CNT-OH) were first treated with maleic anhydride in order to introduce vinylic groups onto the CNT surface (Figure S2), which serves as a coupling agent facilitating the *in situ* polymerization of styrene. Thus a polystyrene (PS) layer was coaxially grown on CNT and further treated with H_2SO_4, to form a sulfonated PS layer coupled with sulfonic groups ($-SO_3^-$). The CNT-SPS with negative charge can absorb various positively-charged metal ions (eg: Ni^{2+}, Co^{2+}, Zn^{2+}) through mutual electrostatic interactions, followed by mineralization and

oxidization during the wet-chemical reaction process and then subsequently calcination. After calcination in nitrogen, delicate TMO@CNT hybrid materials with TMO nanosheets coaxially standing on CNT are produced.

Materials and Methods

Materials. Hydroxyle-group functionalized CNT (denote as CNT-OH, Chengdu Organic Chemicals Co. Ltd), Maleic anhydride, azobisisobutyronitrile (AIBN), methylbenzene, acetone, styrene, sulfuric acid, $Ni(NO_3)_2{\cdot}6H_2O$, $Zn(NO_3)_2{\cdot}6H_2O$, $Co(NO_3)_2{\cdot}6H_2O$, hexamethylenetetramine and citric acid trisodium salt dehydrate were all obtained by Aladdin Ltd. (China) were used as received without further treatment.

Functionalization of CNT with sulfonated polystyrene (PS@CNT). For the growth of transition metal oxide nanosheets on CNT, the as-received CNT-OH was firstly functionalized with sulfonated polystyrene, and the functionalization process is illustrated in Figure S2. Firstly, 0.4 g CNT-OH and 8.25 g maleic anhydride were dispersed in 60 mL acetone by sonication in a round-bottom flask. After stirring for 12 hours at room temperature, the centrifugation black precipitate was washed with dry acetone for several times to remove the organic residue. After dried at 60 °C for 10 hours, 0.127 g of the resultant black product above was re-dispersed in 30 mL anhydrous toluene into a three-necked round-bottom flask. 80 mg AIBN and 4.2 mL styrene mixed solution slowly added into the above suspension and then stirred for 3 h at 70 °C under a nitrogen flow. The cooling down the solution to room temperature naturally. The black precipitate, is the PS@CNT, is collected by centrifugation and washed with ethanol several times. The as-prepared PS@CNT were dried in vacuum at 60 °C overnight for use.

Sulfonation of CNT-PS (CNT-SPS). 3 g CNT-PS was dispersed into a concentrated sulfuric acid (CNT-PS: H_2SO_4 = 1:30, w/w) by sonication, followed by stirring at 40 °C for another 10 min. The sulfonated CNT-PS were obtained by filtering the black precipitate after successively washing with deionized water and ethanol to neutral pH.

Synthesis of transition metal (Ni, Co, Zn) oxide nanosheets on CNT (TMO@CNT). For the synthesis of NiO@CNT, 15 mg CNT-SPS was firstly dispersed in 40 mL deionized water by sonication. 0.5 mmol $Ni(NO_3)_2{\cdot}6H_2O$, 0.25 mmol hexamethylenetetramine and 0.025 mmol citric acid trisodium salt dehydrate were added in above suspension. Then, the mixed solution was heated to 90 °C for 6 h. The product of Ni-precursor@CNT was collected by centrifugation, washed with ethanol several times, and dried at 60 °C for 12 h in vacuum. The NiO@CNT was finally obtained by annealing the Ni-precursor@CNT at 400 °C for 2 h under nitrogen atmosphere with a heating ramp rate of 1 °C min^{-1}. For the synthesis of Co_3O_4@CNT, 0.5 mmol $Ni(NO_3)_2{\cdot}6H_2O$ was simply replaced with 0.5 mmol $Co(NO_3)_2{\cdot}6H_2O$, keeping all other parameters constant, while for the syntheses of $NiCoO_2$@CNT and $ZnCo_2O_4$@CNT, 0.25 mmol $Ni(NO_3)_2{\cdot}6H_2O$ and 0.25 mmol $Co(NO_3)_2{\cdot}6H_2O$, and 0.25 mmol $Zn(NO_3)_2{\cdot}6H_2O$ and 0.5 mmol $Co(NO_3)_2{\cdot}6H_2O$ were used, respectively.

Characterization. FESEM images were obtained by a HITACHI su-8010 microscope and TEM images were obtained by a JEOL JEM-2100 microscope. FT-IR spectrum of the SPS@CNT was characterized by a BRUKER Tensor 27 FT-IR spectrophotometer. The phase structures were examined with SHIMADZU Lab X XRD-6000 X-ray diffractometer. Brunauer-Emmett-Teller (BET) method was applied to measure the specific surface area of the products by nitrogen adsorption–desorption isotherms at 77 K in an Autosorb iQ-MP Surface Area and Pore Size Analyzer (Quantachrome Instruments).

Electrochemical Measurements. For LIB and EC applications, the working electrodes were prepared by spreading a paste containing the active material ($ZnCo_2O_4$@CNT and $NiCoO_2$@CNT), carbon black (super-P-Li) and polymer binder (polyvinylidene difluoride, PVDF, Aldrich) in a weight ratio of 70:20:10.

As electrode for LIBs, 1.1 mg as-prepared $ZnCo_2O_4$ NSs@CNT paste was spread onto a copper foil and then dried at 120 °C overnight in a vacuum oven, followed by pressing at 10 MPa. 1.0 M $LiPF_6$ in ethylene carbonate (EC) and diethyl carbonate (DMC) (50:50, w/w) used as the electrolyte. CR2025 coin cells assembly was carried out in an Ar-filled glovebox. CV tests were performed on an electrochemical workstation (CHI 660E, Chenhua, Shanghai). Galvanostatic charge-discharge measurements were carried out using a battery testing system (NEWARE, Shenzhen).

As electrode for ECs, 2 mg $NiCo_2O_4$ slurry was spread onto a graphite paper of 2 cm^2 and then dried at 120 °C overnight under vacuum. The electrochemical test was conducted with a three-electrode cell in a CHI 660E electrochemical workstation. A Pt electrode as counter electrode, a saturated calomel electrode (SCE) used as the reference electrode, and 2.0 M KOH aqueous solution was used as electrolyte.

The specific capacities were reported based on the amount of the active material, including both TMO nanosheets and CNT, not including the weight of the additives in the electrode.

Results and Discussion

The morphological structure of the CNT coated with a layer of sulfonated polystyrene (SPS-CNT) was examined by scanning electron microscopy (SEM) and transmission electron microscopy (TEM). Figure 2A shows that SPS-CNT displays are randomly aligned with lengths of ~2–5 μm. The TEM image in Fig. 2B shows a single carbon nanotube with a diameter of ~120 nm, on which a very thin layer of SPS with thickness of ~4 nm can be clearly observed. The FT-IR spectrum apparently reveals the presence of SPS layer on the CNT (Fig. 2C). The characteristic bands at 1194, 1138 and 656 cm^{-1} can be assigned to the sulfonic acid group ($-SO_3H$). The band at 1103 cm^{-1} is related to the sulfone group ($-SO_2^-$). Compared with previous reports[43], all the characteristic bands are slightly red-shifted due to the conjugation effect between SPS layer and CNT backbone.

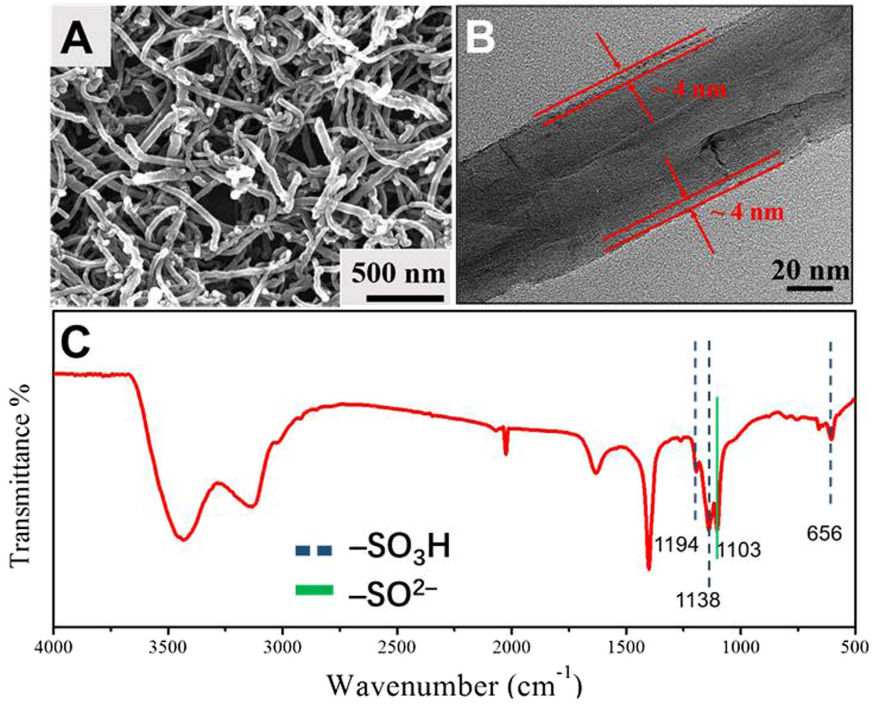

Figure 2. (**A**) SEM image, (**B**) TEM image and (**C**) FT-IR spectrum of SPS-CNT.

After functionalizing CNT with a SPS layer, various sheet-like metal-containing precursors can be easily grown on CNT via a facile solution-based method. The procedure is illustrated in Fig. 3. Even though different transition metal ions such as unitary Ni^{2+}, Co^{2+} and binary Ni^{2+}-Co^{2+} and Zn^{2+}-Co^{2+} were used, Ni-, Co-, NiCo-, and ZnCo-precursor@CNT-SPS composites were successfully prepared with transition metal precursors coaxially grown on the one-dimensional (1D) CNT with increased diameters up to ~150 nm (Fig. 3A,C,E and G). The TEM images taken from single 1D hybrid nanostructures clearly reveal that ultrathin nanosheets stand on the CNTs, despite the slight difference in the size and growth density (Fig. 3B,D,F and H). Such hierarchical nanostructures with nanosheet shells uniformly and coaxially standing on the CNT cores exhibits porous structure with large surface area (Figure S3, Table S1), which may greatly facilitate the exotic chemical transport and interfacial reaction.

To verify the important role of CNT and their functionalization with SPS in the formation of the unique 1D hierarchical composite structure, additional experiments were carried out without the presence of CNT or with pristine CNT (CNT-OH) during the syntheses. When no CNT were added into the reaction systems, only spherical aggregates with mirco-scale size and poor uniformity were obtained, which were composed of densely stacked sheet-like subunits (Figure S4: A, C, E and G). On the other hand, if CNT functionalized with −OH but without SPS layer were introduced for the synthesis, mixtures of CNT and irregularly assembled sheet-like particles were obtained (Figure S4: B, D, F and H). These results demonstrate that the SPS coating on CNT is critical for the successful and coaxial growth of transition metal derivatives on CNT.

The metal-precursors on CNT were confirmed to be metal hydroxide (Figure S5), which needed further annealing in inert gas in order to convert into corresponding metal oxides and maintain their composite structure with CNT. Figure 4 shows the morphologies and microstructures of TMO@CNT composites after annealing at 400 °C for 2 hours under nitrogen flow. It can be observed that the overall morphologies, especially the nanosheet structures of the different TMO@CNT composites are well preserved after annealing, suggesting the excellent thermal stability of the samples (Fig. 4A,D,G and J). Meanwhile, the surfaces become coarse and porous (Fig. 4B,E,H and K) after the thermal decomposition of the TMO-precursors and subsequent recrystallization process. Table S1 compares the BET specific surface areas of the TMO-precursor@CNT and the as-obtained TMO@CNT composites, showing that annealing further enlarged the surface area of these materials with improved chemical stability and activity. The elemental composition and distribution of the TMO@CNT composites were further analyzed by energy-dispersive X-ray spectroscopy (EDS) in scanning transmission electron microscopy (STEM), as shown ordinally in Fig. 4C,F,I and H. The EDS mappings clearly show the different spatial distributions of the two components, namely carbon corresponding to CNT core and metal oxides corresponding to the TMO shell. Carbon is located towards the center region of the hybrid structure and metal oxides mainly cover the outer region, further confirming the uniform core-shell structure.

The crystal phases of the samples were characterized by X-ray diffraction (XRD) (Figure S6). All the samples show a peak at $2\theta = 26°$, corresponding to the (002) diffraction of CNT[9]. In addition, the peak intensity of CNT is less distinguished, suggesting the good coverage of CNT by TMOs and the relatively low CNT content in the composite. Moreover, the metal precursors on CNT were converted into their corresponding oxides. Figure S6A shows that all the other peaks can be indexed to the monoclinic NiO (JCPDS: 47-1049)[44,45], indicating

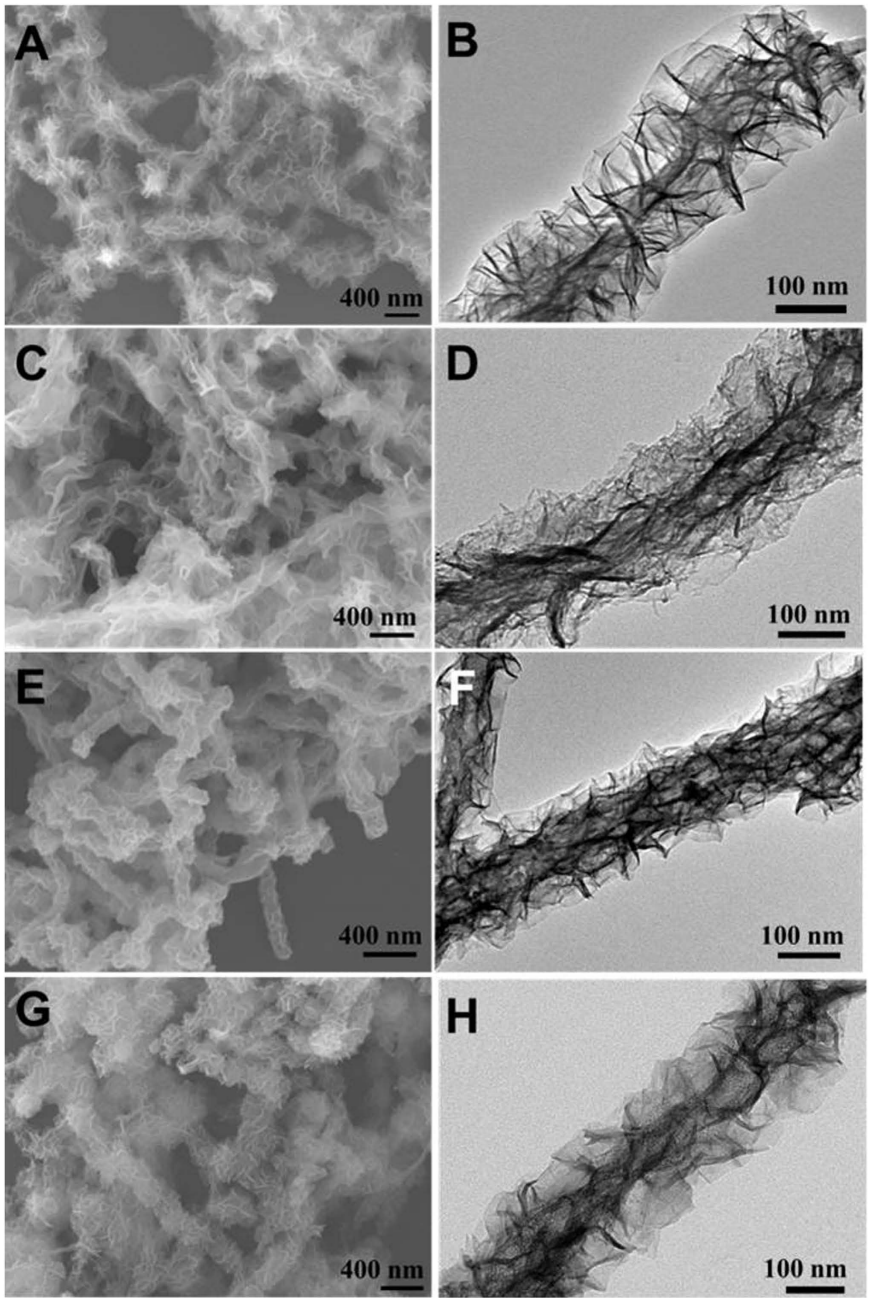

Figure 3. SEM and TEM images of (**A**,**B**) Ni-precursor@CNT, (**C**,**D**) Co-precursor@CNT, (**E**,**F**) NiCo-precursor@CNT and (**G**,**H**) ZnCo-precursor@CNT.

the Ni-precursor@CNT were converted into NiO@CNT after annealing. Similarly, the XRD patterns can be correspondingly assigned to Co_3O_4@CNT (JCPDS: 42-1467, Figure S6B)[46,47], $NiCoO_2$@CNT (JCPDS: 10-0188, Figure S6C)[48,49] and $ZnCo_2O_4$@CNT (JCPDS: 23-1390, Figure S6D)[50].

Electrochemical impedance spectroscopy (EIS) was carried out in order to demonstrate the potential electrochemical applications of such TMO@CNT composites. Figure S10 shows the EIS Nyquist plots of pure TMOs and TMO@CNT composites, in which the charge-transfer resistance of the electrode can be revealed by the semi-circle diameter at the high frequency region. Apparently, all TMO@CNT composites exhibit much smaller electron transfer resistance than that of corresponding pure TMOs, indicating the fast electron transfer after the introduction of electrically conductive CNTs. The ternary oxides of $NiCoO_2$ and $ZnCo_2O_4$ display a smaller semicircle diameter than that of the binary oxides of NiO and Co_3O_4, indicating the improved electron-transfer performance can be achieved by composition engineering of mixed metal oxides, which is consistent with previous reports[50,51].

The as-prepared TMO@CNT composites were examined as electrode materials for LIBs. Among these binary oxides (NiO and Co_3O_4) and ternary oxides ($NiCoO_2$, $ZnCo_2O_4$), $ZnCo_2O_4$ with a higher theoretical capacity[50–52]

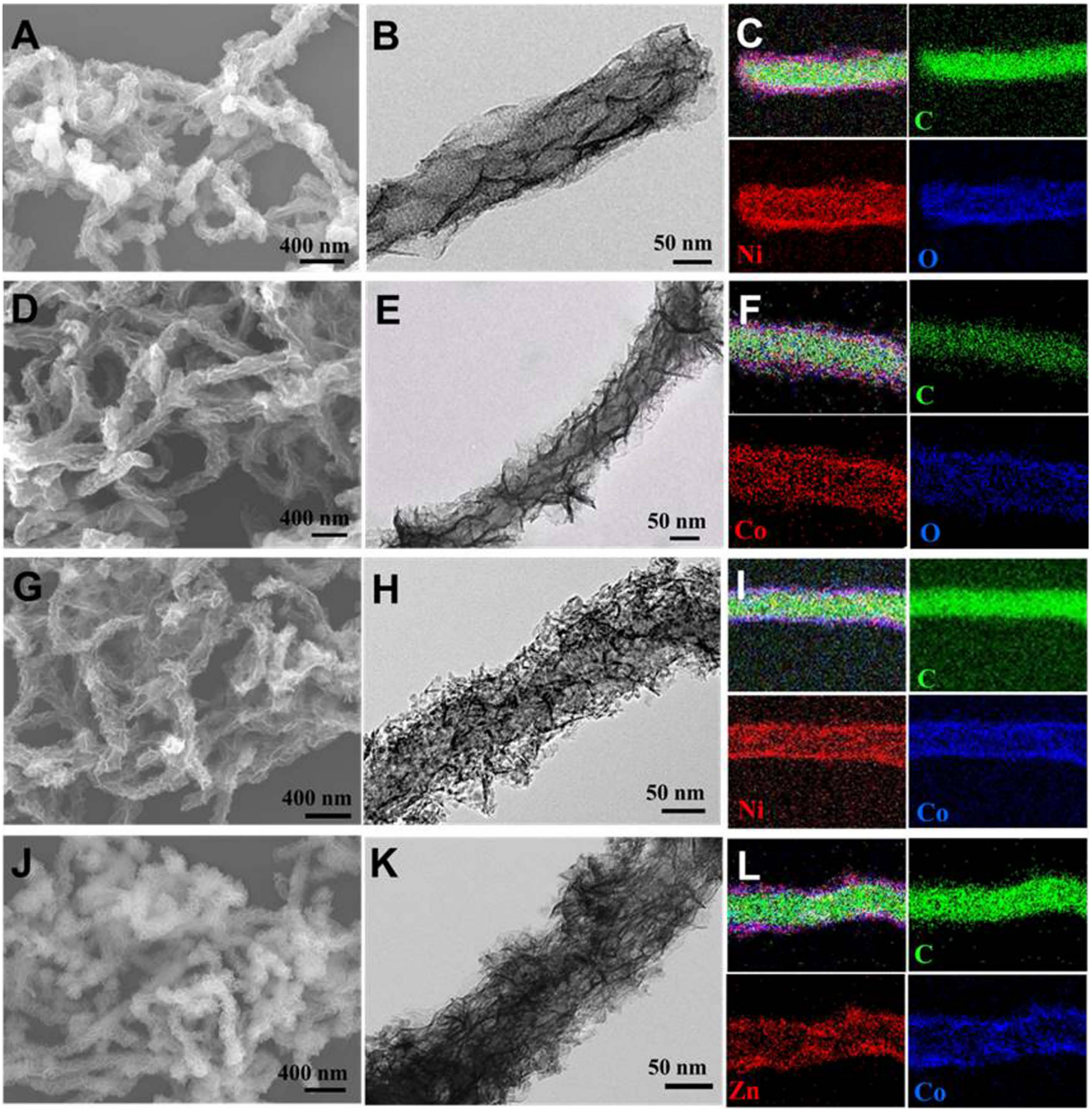

Figure 4. SEM, TEM and EDS mapping images of (**A**,**B** and **C**) NiO@CNT, (**D**,**E** and **F**) Co_3O_4@CNT, (**G**,**H** and **I**) $NiCoO_2$@CNT and (**J**,**K** and **L**) $ZnCo_2O_4$@CNT.

demonstrated the best lithium storage properties when anchoring on the CNT as electrode. Figure 5A depicts the cyclic voltammograms (CVs) of the electrode made from the $ZnCo_2O_4$@CNT for the initial three cycles at a scan rate of 0.5 mVs^{-1}. In the first cycle, the intense peak located at ~0.53 V can be assigned to the reduction of Co^{3+} and Zn^{2+} to metallic Co and Zn, as well as the formation of a solid electrolyte interface (SEI)[14,50,51]. In the following anodic scan, there are two oxidation peaks appeared at ~1.7 V and ~2.1 V, which can be attributed to the oxidation process of metallic Zn and Co, respectively. The charge and discharge processes can be described as follows[50,51,53–55]:

$$ZnCo_2O_4 + 8Li^+ + 8e^- \leftrightarrow Zn + 2Co + 4Li_2O \quad (1)$$

$$Zn + Li^+ + e^- \leftrightarrow LiZn \quad (2)$$

$$Zn + Li_2O \leftrightarrow ZnO + 2Li^+ + 2e^- \quad (3)$$

$$Co + Li_2O \leftrightarrow CoO + 2Li^+ + 2e^- \quad (4)$$

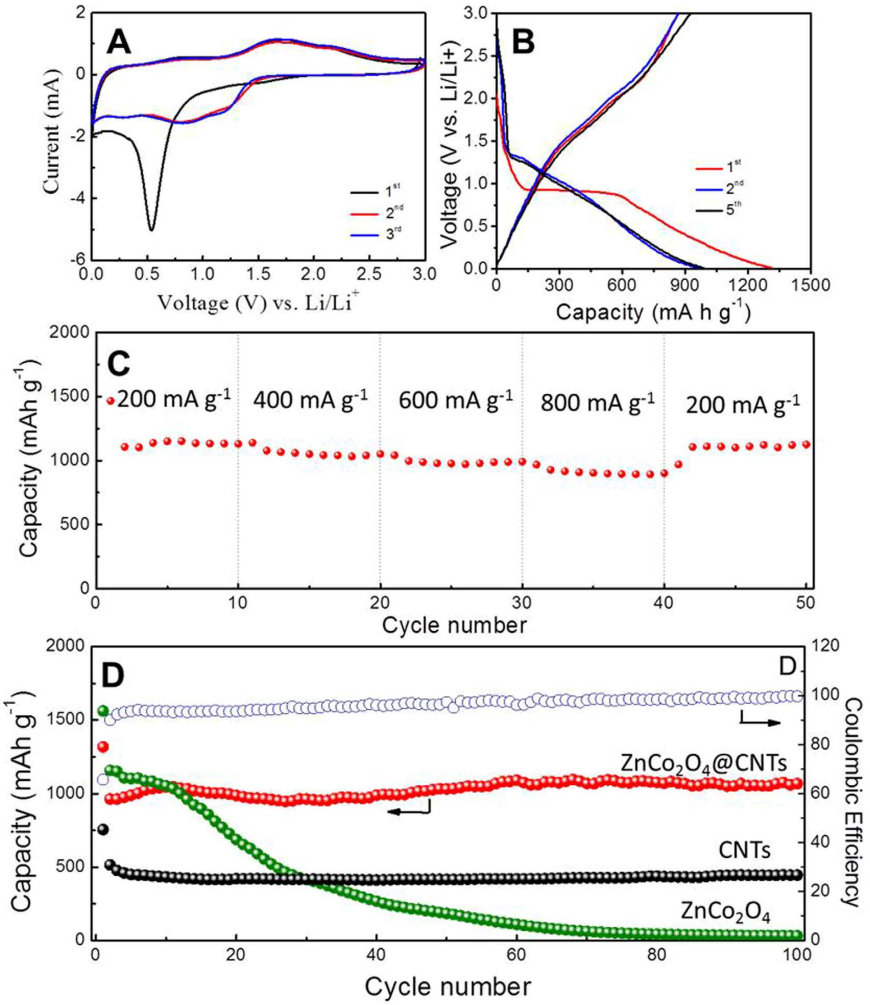

Figure 5. (**A**) CV curves of the $ZnCo_2O_4$@CNT electrode at a scan rate of 0.5 mVs^{-1} between 0.01 V and 3.0 V. (**B**) Charge-discharge voltage profiles of the $ZnCo_2O_4$@CNT electrode at a current density of 400 mAg^{-1}. (**C**) Rate capability of $ZnCo_2O_4$@CNT electrode at different current densities. (**D**) Comparison of cycling performance of $ZnCo_2O_4$@CNT (curve I), CNT (curve II) and pure $ZnCo_2O_4$ (curve III) at a current density of 400 mAg^{-1}. Curve IV shows the corresponding coulombic efficiency of the $ZnCo_2O_4$@CNT electrode.

$$3CoO + Li_2O \leftrightarrow Co_3O_4 + Li^+ + e^- \quad (5)$$

Figure 5B presents the charge-discharge voltage profiles of $ZnCo_2O_4$@CNT for the 1st, 2nd and 5th cycles. Coinciding with the CV analysis above, there are two slanted platform with gradually decreasing voltage appeared. The initial discharge and charge capacities are 1317 mAh g^{-1} and 865 mAh g^{-1} at 200 mAg^{-1}, respectively. The irreversible capacity loss during the first cycle is about 452 mAh g^{-1}, which can be attributed to the incomplete decomposition of a SEI film[56–59].

Figure 5C shows that the $ZnCo_2O_4$@CNT electrode exhibits excellent rate capability at different current densities. Benefitted from the unique structure, even at a high current density of 800 mAg^{-1}, the $ZnCo_2O_4$@CNT electrode still deliver a discharge capacity of 900 mAh g^{-1}. Figure 5D depicts the comparative cycling performance of three different samples: pure commercial CNT, pure $ZnCo_2O_4$ and $ZnCo_2O_4$@CNT at the same current density of 400 mAg^{-1}. The $ZnCo_2O_4$@CNT electrode shows an excellent stable cycling performance of 1068 mAh g^{-1} after 100 cycles. Whereas, the pure $ZnCo_2O_4$ electrode shows a rapidly decreasing along with cycling, only retaining 33.8 mAh g^{-1} after the same cycles, while CNT electrode exhibit a lower reversible capacity of 490 mAh g^{-1}. Apparently, the $ZnCo_2O_4$@CNT electrode manifests the best cycling performance. The excellent lithium storage properties of $ZnCo_2O_4$@CNT can be attributed to the unique composite structure. On one hand, CNT possess good electrical conductivity, high mechanical strength and flexibility, facilitating the efficient charge transfer and maintaining the structural integrity of the electrode during the repeating charge-discharge processes. On the other hand, the ultrathin $ZnCo_2O_4$ nanosheets coaxially standing on CNT provide numerous active sites for lithium storage due to their large surface area. The combination of the high lithium storage capacity of TMOs and the buffering effect of conductive CNT matrix contributes to an enhanced electrochemical performance[29]. Besides, we also investigate the lithium storage properties of NiO@CNT (Figure S7), Co_3O_4@CNT (Figure S8)

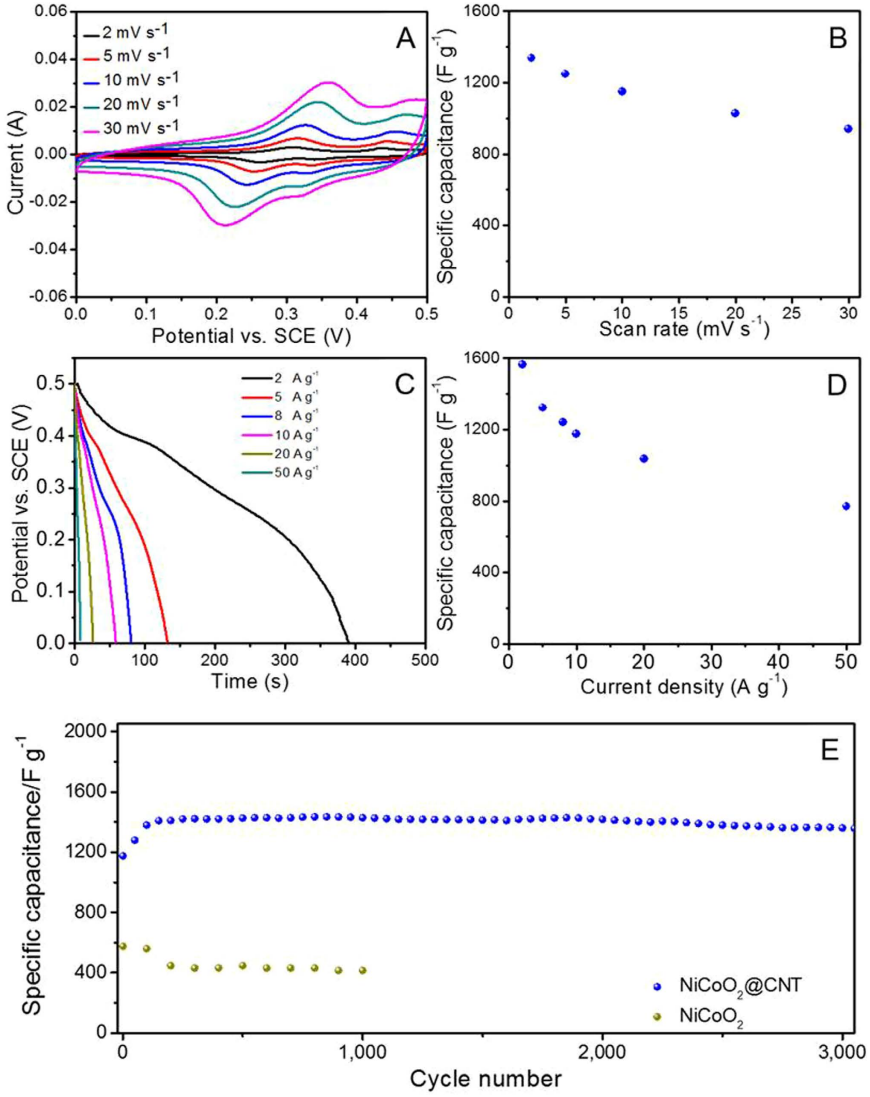

Figure 6. Electrochemical characterization of $NiCoO_2$@CNT. (**A**) CV curves at various scan rates ranging from 2 to 30 mVs^{-1}. (**B**) average specific capacitance of $NiCoO_2$@CNT at various scan rates. (**C**) Discharge voltage profiles at various scan rates ranging from 2 to 50 Ag^{-1}. (**D**) The calculated capacitance as a function of current density according to data in (**C**). (**E**) Specific capacitance versus cycle number of $NiCoO_2$@CNT at a current density of 10 Ag^{-1}.

and $NiCoO_2$@CNT (Figure S9) electrodes and prove whole these materials exhibiting superior capacitances and nice stabilities.

Electrochemical capacitors are an alternative type of device which can storage and release energy rapidly and reversibly[2,3,60]. The electrochemical capacitive properties of TMOs and TMO@CNT composites were also investigated and the as-prepared $NiCoO_2$@CNT was found to demonstrate the best performance. Figure 6A shows the CV curves of the $NiCoO_2$@CNT electrode at scan rates from 2 to 50 mVs^{-1}. The shape of the CV curves reveals the typical pseudocapacitive characteristics of the sample. One pair of redox peaks within the potential range from 0 to 0.5 V vs. a saturated calomel electrode (SCE). It can be attributed to the reversible reduction as described by reactions (6) and (7) below[61]:

$$NiCoO_2 + 2OH^- \leftrightarrow NiOOH + CoOOH + 2e^- \quad (6)$$

$$CoOOH + OH^- \leftrightarrow CoO_2 + H_2O + e^- \quad (7)$$

Along with the rate increasing, except for a little shift of the peaks position, the shape of CV curves shows no significant change, thus indicating great electrochemical reversibility and excellent rate performance. As shown in Fig. 6B, the average capacitances of $NiCoO_2$@CNT are calculated to be 1335, 1248, 1150, 1025 and 939 Fg^{-1} at scan rates of 2, 5, 10, 20 and 30 mVs^{-1}, respectively. Figure 6C shows the galvanostatic discharge curves of the $NiCoO_2$@CNT at different current densities ranging from 2 to 50 Ag^{-1}. There are two clear plateaus appearing in

each discharge curve, which are consistent with the CV analysis. Each specific capacitance at different rate can be calculated via equation (8):

$$C_m = I \times \Delta t/(\Delta V \times m) \quad (8)$$

where C_m (F g^{-1}) is the specific capacitance, I (A) is the discharge current, Δt (s) is the discharge time, ΔV is the potential change during the discharge process, and the m (g) is the mass of the active materials ($NiCoO_2$@CNT) in the electrode. The calculated specific capacitance at different discharge current density shown in Fig. 6D, giving high specific capacitances of 1564, 1322, 1240, 1176, and 1036 Fg^{-1} at different current densities of 2, 5, 8, 10, 20 and 50 Ag^{-1}, respectively. Figure 6E display the specific capacitance at a current density of 10 Ag^{-1} of 3000 cycles for investigating the performance of cycling stability. The specific capacitance is around 1176 Fg^{-1} in the first cycle, and it slightly increases to 1380 Fg^{-1} in the course of first 100 cycles, which still keeps a capacitance of 1360 Fg^{-1} after 3000 cycles with an overall capacitance loss of only 1.4%. The excellent electrochemical performance further highlights the capability of the $NiCoO_2$@CNT composite electrode to meet the requirements of both long cycling performance and good rate capability, which are promising for practical application as energy storage devices.

In summary, we have developed a general strategy to synthesize various TMO@CNT composite materials with the assistance of pre-coated sulfonated-polystyrene (SPS) layers on CNT. The SPS layer effectively facilitate the growth of metal-precursor nanosheets under wet-chemical synthesis, which can be conformably converted into metal oxide nanosheets by annealing under inert atmosphere, leading to the formation of core-shell hybrid hierarchical nanostructures. Owing to the unique hybrid nanostructure and strong coupling effect between CNT and TMOs, improved charge transfer process and large active surface area are achieved, which results in excellent electrochemical lithium/charge storage properties when evaluated as electrode materials for lithium ion batteries and electrochemical capacitors. More importantly, the general synthetic approach allows the readily engineering of compositions of the shell components with delicate morphologies on CNT, which would be greatly promising to explore advanced functional materials with potential applications in various emerging technologies, such as energy storage/conversion systems, electronic devices, and sensors.

References

1. Iijima, S. Helical Microtubules of Graphitic Carbon. *Nature* **354,** 56–58 (1991).
2. Benson, J. *et al.* Multifunctional CNT-Polymer Composites for Ultra-Tough Structural Supercapacitors and Desalination Devices. *Adv. Mater.* **25,** 6625–6632 (2013).
3. Xiao, X. *et al.* Freestanding Mesoporous VN/CNT Hybrid Electrodes for Flexible All-Solid-State Supercapacitors. *Adv. Mater.* **25,** 5091–5097 (2013).
4. Ding, S. J., Chen, J. S. & Lou, X. W. CNTs@SnO_2@Carbon Coaxial Nanocables with High Mass Fraction of SnO_2 for Improved Lithium Storage. *Chem. Asian. J.* **6,** 2278–2281 (2011).
5. Sun, H., Deng, J., Qiu, L., Fang, X. & Peng, H. Recent progress in solar cells based on one-dimensional nanomaterials. *Energ. Environ. Sci.* **8,** 1139–1159 (2015).
6. Jian, Z. L. *et al.* Core-Shell-Structured CNT@RuO_2 Composite as a High-Performance Cathode Catalyst for Rechargeable Li-O_2 Batteries. *Angew. Chem. Int. Ed.* **53,** 442–446 (2014).
7. Xiao, C., Zou, Q. & Tang, Y. Surface nitrogen-enriched carbon nanotubes for uniform dispersion of platinum nanoparticles and their electrochemical biosensing property. *Electrochim. Acta* **143,** 10–17 (2014).
8. Tatami, J., Katashima, T., Komeya, K., Meguro, T. & Wakihara, T. Electrically Conductive CNT-Dispersed Silicon Nitride Ceramics. *J. Am. Ceram. Soc.* **88,** 2889–2893 (2005).
9. Liu, Q., Tian, J. *et al.* Carbon Nanotubes Decorated with CoP Nanocrystals: A Highly Active Non-Noble-Metal Nanohybrid Electrocatalyst for Hydrogen Evolution. *Angew. Chem. Int. Ed.* **53,** 6710–6714 (2014).
10. Li, X. *et al.* Enhanced activity and durability of platinum anode catalyst by the modification of cobalt phosphide for direct methanol fuel cells. *Electrochim. Acta* **185,** 178–183 (2015).
11. Andersen, N. I., Serov, A. & Atanassov, P. Metal oxides/CNT nano-composite catalysts for oxygen reduction/oxygen evolution in alkaline media. *Appl. Catal. B Environ.* **163,** 623–627 (2015).
12. Ding, S., Chen, J. S. & Lou, X. W. D. Glucose-Assisted Growth of MoS_2 Nanosheets on CNT Backbone for Improved Lithium Storage Properties. *Chem. Eur. J.* **17,** 13142–13145 (2011).
13. Ding, S. J. *et al.* Graphene-supported anatase TiO_2 nanosheets for fast lithium storage. *Chem. Commun.* **47,** 5780–5782 (2011).
14. Mohamed, S. G. *et al.* Flower-like $ZnCo_2O_4$ nanowires: toward a high-performance anode material for Li-ion batteries. *RSC Adv.* **3,** 20143–20149 (2013).
15. Fujigaya, T. & Nakashima, N. Fuel Cell Electrocatalyst Using Polybenzimidazole-Modified Carbon Nanotubes As Support Materials. *Adv. Mater.* **25,** 1666–1681 (2013).
16. Yi, H., Wang, H., Jing, Y., Peng, T. & Wang, X. Asymmetric supercapacitors based on carbon nanotubes@ NiO ultrathin nanosheets core-shell composites and MOF-derived porous carbon polyhedrons with super-long cycle life. *J. Power Sources* **285,** 281–290 (2015).
17. Poizot, P., Laruelle, S., Grugeon, S., Dupont, L. & Tarascon, J. M. Nano-sized transition-metaloxides as negative-electrode materials for lithium-ion batteries. *Nature* **407,** 496–499 (2000).
18. Lai, X. *et al.* General Synthesis and Gas-Sensing Properties of Multiple-Shell Metal Oxide Hollow Microspheres. *Angew. Chem. Int. Ed.* **50,** 2738–2741 (2011).
19. Zu, G. *et al.* Highly Thermally Stable, Core–Shell Nanostructured Metal Oxide Aerogels as High-Temperature Thermal Superinsulators, Adsorbents, and Catalysts. *Chem. Mater.* **26,** 5761–5772 (2014).
20. Cao, X. *et al.* Preparation of novel 3D graphene networks for supercapacitor applications. *Small* **7,** 3163–3168 (2011).
21. Liang, Y. *et al.* Co_3O_4 nanocrystals on graphene as a synergistic catalyst for oxygen reduction reaction. *Nat. Mater.* **10,** 780–786 (2011).
22. Huang, L. *et al.* Nickel–cobalt hydroxide nanosheets coated on $NiCo_2O_4$ nanowires grown on carbon fiber paper for high-performance pseudocapacitors. *Nano Lett.* **13,** 3135–3139 (2013).
23. Raccichini, R., Varzi, A., Passerini, S. & Scrosati, B. The role of graphene for electrochemical energy storage. *Nat. Mater.* **14,** 271–279 (2015).
24. Yuan, C. *et al.* Heterostructured core–shell $ZnMn_2O_4$ nanosheets@carbon nanotubes' coaxial nanocables: a competitive anode towards high-performance Li-ion batteries. *Nanotechnology* **26,** 145401 (2015).

25. Huang, H. *et al.* Self-assembly of mesoporous CuO nanosheets–CNT 3D-network composites for lithium-ion batteries. *Nanoscale* **5,** 1785–1788 (2013).
26. Ning, G. *et al.* Three-dimensional hybrid materials of fish scale-like polyaniline nanosheet arrays on graphene oxide and carbon nanotube for high-performance ultracapacitors. *Carbon* **54,** 241–248 (2013).
27. Wang, C.-C., Chang, Y.-J., Hsieh, Y.-C. & Lin, Y.-T. Sensible heat and friction characteristics of plate fin-and-tube heat exchangers having plane fins. *Int. J. Refrig.* **19,** 223–230 (1996).
28. Wang, C., Fu, W. & Chang, C. Heat transfer and friction characteristics of typical wavy fin-and-tube heat exchangers. *Exp. Therm. Fluid Sci.* **14,** 174–186 (1997).
29. Ding, S. J., Chen, J. S. & Lou, X. W. One-Dimensional Hierarchical Structures Composed of Novel Metal Oxide Nanosheets on a Carbon Nanotube Backbone and Their Lithium-Storage Properties. *Adv. Funct. Mater.* **21,** 4120–4125 (2011).
30. Fang, X. *et al.* Lithium storage in commercial MoS_2 in different potential ranges. *Electrochim. Acta* **81,** 155–160 (2012).
31. Chen, S., Zhu, J., Zhou, H. & Wang, X. One-step synthesis of low defect density carbon nanotube-doped $Ni(OH)_2$ nanosheets with improved electrochemical performances. *RSC Adv.* **1,** 484–489 (2011).
32. Zhong, J. L. *et al.* Ultrathin NiO nanoflakes perpendicularly oriented on carbon nanotubes as lithium ion battery anode. *J. Mater. Res.* **28,** 2577–2583 (2013).
33. Liu, J. *et al.* Fullerene pipes. *Science* **280,** 1253–1256 (1998).
34. Datsyuk, V. *et al.* Chemical oxidation of multiwalled carbon nanotubes. *Carbon* **46,** 833–840 (2008).
35. Chen, J. *et al.* Solution properties of single-walled carbon nanotubes. *Science* **282,** 95–98 (1998).
36. Srivastava, M. *et al.* Recent advances in graphene and its metal-oxide hybrid nanostructures for lithium-ion batteries. *Nanoscale* **7,** 4820–4868 (2015).
37. Du, N. *et al.* Porous indium oxide nanotubes: Layer-by-layer assembly on carbon-nanotube templates and application for room-temperature NH_3 gas sensors. *Adv. Mater.* **19,** 1641–+ (2007).
38. Yang, M., Ma, J., Zhang, C., Yang, Z. & Lu, Y. General synthetic route toward functional hollow spheres with double-shelled structures. *Angew. Chem. Int. Ed.* **44,** 6727–6730 (2005).
39. Yang, Z., Niu, Z., Lu, Y., Hu, Z. & Han, C. C. Templated synthesis of inorganic hollow spheres with a tunable cavity size onto core-shell gel particles. *Angew. Chem. Int. Ed.* **42,** 1943–1945 (2003).
40. Li, J. J., Ding, S. J., Zhang, C. L. & Yang, Z. Z. Synthesis of composite eccentric double-shelled hollow spheres. *Polymer* **50,** 3943–3949 (2009).
41. Ding, S. J. *et al.* Controlled synthesis of hierarchical NiO nanosheet hollow spheres with enhanced supercapacitive performance. *J. Mater. Chem.* **21,** 6602–6606 (2011).
42. Ding, S. J. *et al.* TiO_2 hollow spheres with large amount of exposed (001) facets for fast reversible lithium storage. *J. Mater. Chem.* **21,** 1677–1680 (2011).
43. Ding, S. J. *et al.* Template synthesis of composite hollow spheres using sulfonated polystyrene hollow spheres. *Polymer* **47,** 8360–8366 (2006).
44. Wang, X. *et al.* Optical and electrochemical properties of nanosized NiO via thermal decomposition of nickel oxalate nanofibres. *Nanotechnology* **16,** 37 (2005).
45. Xu, Y. F., Gao, M. R., Zheng, Y. R., Jiang, J. & Yu, S. H. Nickel/Nickel (II) Oxide Nanoparticles Anchored onto Cobalt (IV) Diselenide Nanobelts for the Electrochemical Production of Hydrogen. *Angew. Chem. Int. Ed.* **52,** 8546–8550 (2013).
46. Xia, X.-H., Tu, J.-P., Wang, X.-L., Gu, C.-D. & Zhao, X.-B. Mesoporous Co_3O_4 monolayer hollow-sphere array as electrochemical pseudocapacitor material. *Chem. Commun.* **47,** 5786–5788 (2011).
47. Na, C. W., Woo, H.-S., Kim, I.-D. & Lee, J.-H. Selective detection of NO_2 and C_2H_5OH using a Co_3O_4-decorated ZnO nanowire network sensor. *Chem. Commun.* **47,** 5148–5150 (2011).
48. Zhang, X. *et al.* Electrochemical sensor based on carbon-supported $NiCoO_2$ nanoparticles for selective detection of ascorbic acid. *Biosens. Bioelectron.* **55,** 446–451 (2014).
49. Liu, Y. *et al.* Hierarchical $CoNiO_2$ structures assembled from mesoporous nanosheets with tunable porosity and their application as lithium-ion battery electrodes. *New J. Chem.* (2014).
50. Sharma, Y., Sharma, N., Subba Rao, G. & Chowdari, B. Nanophase $ZnCo_2O_4$ as a High Performance Anode Material for Li-Ion Batteries. *Adv. Funct. Mater.* **17,** 2855–2861 (2007).
51. Liu, B. *et al.* Hierarchical Three-Dimensional $ZnCo_2O_4$ Nanowire Arrays/Carbon Cloth Anodes for a Novel Class of High-Performance Flexible Lithium-Ion Batteries. *Nano Lett.* **12,** 3005–3011 (2012).
52. Sun, Z. *et al.* Facile fabrication of hierarchical $ZnCo_2O_4$/NiO core/shell nanowire arrays with improved lithium-ion battery performance. *Nanoscale* **6,** 6563–6568 (2014).
53. Qiu, Y. C., Yang, S. H., Deng, H., Jin, L. M. & Li, W. S. A novel nanostructured spinel $ZnCo_2O_4$ electrode material: morphology conserved transformation from a hexagonal shaped nanodisk precursor and application in lithium ion batteries. *J. Mater. Chem.* **20,** 4439–4444 (2010).
54. Du, N. *et al.* Porous $ZnCo_2O_4$ nanowires synthesis via sacrificial templates: high-performance anode materials of Li-ion batteries. *Inorg. Chem.* **50,** 3320–3324 (2011).
55. Reddy, M. V. *et al.* Nano-$ZnCo_2O_4$ Material Preparation by Molten Salt Method and Its Electrochemical Properties for Lithium Batteries. *J. Electrochem. Soc.* **158,** A1423–A1430 (2011).
56. Chan, C. K., Zhang, X. F. & Cui, Y. High capacity Li ion battery anodes using Ge nanowires. *Nano Lett.* **8,** 307–309 (2008).
57. Spotnitz, R. Simulation of capacity fade in lithium-ion batteries. *J. Power Sources* **113,** 72–80 (2003).
58. Schmidt, A. P., Bitzer, M., Imre, Á. W. & Guzzella, L. Model-based distinction and quantification of capacity loss and rate capability fade in Li-ion batteries. *J. Power Sources* **195,** 7634–7638 (2010).
59. Szczech, J. R. & Jin, S. Nanostructured silicon for high capacity lithium battery anodes. *Energ. Environ. Sci.* **4,** 56–72 (2011).
60. Wu, Z. S. *et al.* Three-dimensional graphene-based macro- and mesoporous frameworks for high-performance electrochemical capacitive energy storage. *J. Am. Chem. Soc.* **134,** 19532–19535 (2012).
61. Xu, X. *et al.* The facile synthesis of hierarchical $NiCoO_2$ nanotubes comprised ultrathin nanosheets for supercapacitors. *J. Power Sources* **267,** 641–647 (2014).

Acknowledgements

This work was supported partially by the National Natural Science Foundation of China (No. 51273158, 21303131). The authors are grateful to the Fundamental Research Funds for the Central Universities for financial support.

Author Contributions

H.Z. and L.S.Z. carried out the synthesis and performed the electrochemical measurements. H.Z., L.S.Z., D.Y.Z., S.Q.C. and P.R.C. carried out the materials characterization. H.Z., L.S.Z., X.H. M.B. and H.-K. K. provided technical support. H.Z., S.J.D. and K.X. wrote the manuscript. S.J.D. and K.X. supervised the work. All the authors reviewed the manuscript.

Additional Information

Supplementary information accompanies this paper at http://www.nature.com/srep

Competing financial interests: The authors declare no competing financial interests.

How to cite this article: Zhou, H. *et al.* A universal synthetic route to carbon nanotube/transition metal oxide nano-composites for lithium ion batteries and electrochemical capacitors. *Sci. Rep.* **6**, 37752; doi: 10.1038/srep37752 (2016).

Publisher's note: Springer Nature remains neutral with regard to jurisdictional claims in published maps and institutional affiliations.